

CT Radiomic Nomogram Using Optimal Volume of Interest for Preoperatively Predicting Invasive Mucinous Adenocarcinomas in Patients with Incidental Pulmonary Nodules: A Multicenter, Large-Scale Study

Technology in Cancer Research & Treatment
Volume 23: 1-11
© The Author(s) 2024
Article reuse guidelines:
sagepub.com/journals-permissions
DOI: 10.1177/15330338241308307
journals.sagepub.com/home/tct



Zhichao Zuo, MS^{1,†} , Guochao Zhang, MD^{2,†}, Jing Chen, MD^{3,†}, Qi Xue, MD², Shanyue Lin, BS⁴, Ying Zeng, MS¹, Wu Ge, MS¹, Wanyin Qi, BS³, Lu Yang, PhD³, Haibo Liu, BS¹, Xiaohong Fan, PhD⁵, and Shuangping Zhang, MD⁶

Abstract

Introduction: This study evaluated the efficacy of radiomic analysis with optimal volumes of interest (VOIs) on computed tomography images to preoperatively differentiate invasive mucinous adenocarcinoma (IMA) from non-mucinous adenocarcinoma (non-IMA) in patients with incidental pulmonary nodules (IPNs). **Methods:** This multicenter, large-scale retrospective study included 1383 patients with IPNs, 110 (8%) of whom were pathologically diagnosed with IMA postoperatively. Radiomic features were extracted from multi-scale VOI subgroups (VOI^{-2 mm}, VOI^{entire}, VOI^{+2 mm}, and VOI^{+4 mm}). Resampling methods, specifically, the synthetic minority oversampling technique, addressed the imbalance between the majority (IMA) and minority (non-IMA) groups. Radiomic features were identified using the least absolute shrinkage and selection operator algorithm. Radscores were calculated by linearly combining the selected features with their weights. A combined nomogram integrating the optimal VOI-based radiomic model with the image-finding classifier was constructed. **Results:** Bubble lucency and lower lobe predominance were significant in establishing an image-finding classifier to differentiate between IMA and non-IMA in IPNs, achieving an area under the curve (AUC) value of 0.684 (0.568-0.801). Across all radiomic models, IMA had a higher Radscore than did non-IMA. Specifically, the VOI + 2 mm-based radiomic model exhibited the highest performance, with an AUC of 0.832 (0.753-0.911). The combined nomogram outperformed the recognized image-finding classifier and radiomic models, achieving an AUC of 0.850 (0.776-0.925). **Conclusion:** A nomogram that combines a recognized image-finding classifier with an optimal VOI-based radiomic model effectively predicts IMA in IPNs, aiding physicians in developing comprehensive treatment strategies.

¹ Department of Radiology, Xiangtan Central Hospital, Xiangtan, P. R. China

² Department of Thoracic Surgery, National Cancer Center/National Clinical Research Center for Cancer/Cancer Hospital, Chinese Academy of Medical Sciences and Peking Union Medical College, Beijing, P. R. China

³ Department of Radiology, The Affiliated Hospital of Southwest Medical University, Luzhou, P. R. China

⁴ Department of Radiology, Affiliated Hospital of Guilin Medical University, Guilin, P. R. China

⁵ College of Mathematical Medicine, Zhejiang Normal University, Jinhua, P. R. China

⁶ Department of Thoracic Surgery, Shanxi Province Cancer Hospital, Shanxi Hospital Affiliated to Cancer Hospital, Chinese Academy of Medical Sciences, Affiliated Tumor Hospital of Shanxi Medical University, Taiyuan, P. R. China

[†] These authors contributed equally to this work.

Corresponding Authors:

Xiaohong Fan, College of Mathematical Medicine, Zhejiang Normal University, Jinhua 321004, P. R. China.

Email: fanxiaohong@zjnu.edu.cn

Shuangping Zhang, Department of Thoracic Surgery, Shanxi Province Cancer Hospital, Shanxi Hospital Affiliated to Cancer Hospital, Chinese Academy of Medical Sciences, Affiliated Tumor Hospital of Shanxi Medical University, Taiyuan, 030013, P. R. China.

Email: zsp5500@163.com



Creative Commons Non Commercial CC BY-NC: This article is distributed under the terms of the Creative Commons Attribution-NonCommercial 4.0 License (<https://creativecommons.org/licenses/by-nc/4.0/>) which permits non-commercial use, reproduction and distribution of the work without further permission provided the original work is attributed as specified on the SAGE and Open Access page (<https://us.sagepub.com/en-us/nam/open-access-at-sage>).

Keywords

incidental pulmonary nodules, invasive mucinous adenocarcinoma, invasive non-mucinous adenocarcinoma, optimal VOI, radiomics

Received: July 30, 2024; Revised: November 15, 2024; Accepted: November 25, 2024.

Introduction

Detection rates for incidental pulmonary nodules (IPNs) have significantly increased with the widespread adoption of thin-slice computed tomography (CT). IPNs can be categorized into three types: solid nodule (SN), subsolid nodule (SSN), and ground-glass nodule (GGN), depending on their density on the CT images. Among these, IPNs exhibiting malignant characteristics on CT are suspected to be Lung-RADS category 4 lesions. Further, postoperative pathological examination has primarily revealed that most of these lesions are lung adenocarcinomas (LADCs).¹ Among LADC variants, invasive mucinous adenocarcinoma (IMA) represents a distinct subtype, accounting for approximately 5%–10% cases.^{2,3} IMA is characterized by invasive growth patterns of columnar or goblet cells with basally located nuclei and abundant intracytoplasmic mucin, differentiating it from non-mucinous adenocarcinoma (non-IMA).^{2,3} Recognizing these features, the World Health Organization officially classified IMA as a distinct LADC subtype in 2015.⁴

Compared with non-IMA, IMA displays distinct biological characteristics resulting from unique genomic, pathological, and prognostic features. Histologically, IMA is associated with reduced lymphatic permeation, pleural involvement, and vascular invasion while exhibiting a higher tendency for air space spread.^{5–7} Pathologically, patients with IMA present specific mutation patterns in genes such as *EGFR*, *ALK*, and *KRAS*.^{8–11} Targeted therapies are promising options for IMA treatment. Moreover, patients with IMA exhibit a prognosis that is between the prognosis of patients with low- and intermediate-grade non-IMA, closely aligning with that of patients with intermediate-grade non-IMA.¹² Additionally, compared with patients with non-IMA, those with IMA exhibit a higher risk of intrapulmonary recurrence, which affects their prognosis.¹³

Previous studies have extensively investigated IMA imaging features, classifying them into two main types based on CT characteristics: solitary and pneumonic.^{14–16} Pneumonia-type IMA shows significantly poorer overall survival and disease-free survival rates than does solitary-type IMA, despite the latter being more commonly encountered.^{14–16} Solitary-type IMA is typically detected as IPNs on CT images. However, conventional morphological features on CT lack distinctive characteristics, posing significant challenges for accurate diagnosis.¹⁷

Radiomics, a field involving extraction and analysis of data from medical images, helps uncover latent patterns within images, facilitating a more comprehensive understanding of tumor phenotypes.¹⁸ Zhang et al¹⁹ illustrated the enhanced

predictive capability of a composite model that incorporates CT findings and radiomic features for predicting IMA. Additionally, Xiao et al²⁰ developed a radiomic model utilizing various machine learning algorithms, which showed remarkable efficacy in differentiating between IMA and non-IMA. However, these studies primarily focused on characteristics extracted solely from the intratumoral subgroup, potentially overlooking variations in the peritumoral parenchyma. Investigation of peritumoral radiomic features has garnered increasing attention because of their potential to capture migration, invasion, and microenvironmental changes, all common attributes of malignancies. Furthermore, the presence of necrotic or hypoxic regions within the central tumor, alongside predominant cancer cell proliferation in the peripheral tumor, highlights the significance of peritumoral analysis. Several studies have successfully derived radiomic features from intratumoral and peritumoral pulmonary parenchyma, enhancing diagnostic accuracy for predicting various aspects of LADC, including preoperative lymphovascular invasion,²¹ lymph node metastasis,²² and *EGFR* mutation status.²³ However, the current literature lacks evidence from systematic evaluation of radiomic models across multi-scale peritumoral ranges for distinguishing non-IMA from IMA.

To achieve successful radiomic outcomes, developing predictive models with high accuracy, reliability, and efficiency is crucial. Therefore, a multicenter, large-scale study was conducted to ensure the robustness and predictive power of the models. The aim of this study was to explore the impact of multi-scale intratumoral and peritumoral ranges on preoperative IMA prediction by adjusting radial distances at -2 , 2 , and 4 mm from the tumor boundary. Furthermore, this study focused on deriving radiomic features from intratumoral and peritumoral parenchyma using various volumes of interest (VOIs). The optimal VOI was determined through a comprehensive comparison, enabling the selection of the most effective combination for constructing a nomogram. The goal of this nomogram is to serve as a potent tool for accurately predicting IMA in IPNs.

Methods

Patient Selection

This retrospective study was approved by the Ethics Committees of the participating hospitals (reference numbers: KY2020147, 2021-07-009, and 22/244-3446) and conducted in accordance with the Declaration of Helsinki. All research procedures strictly adhered to the relevant guidelines and regulations, and written informed consent was obtained from all participants. Between June 2018 and June 2023, patients with

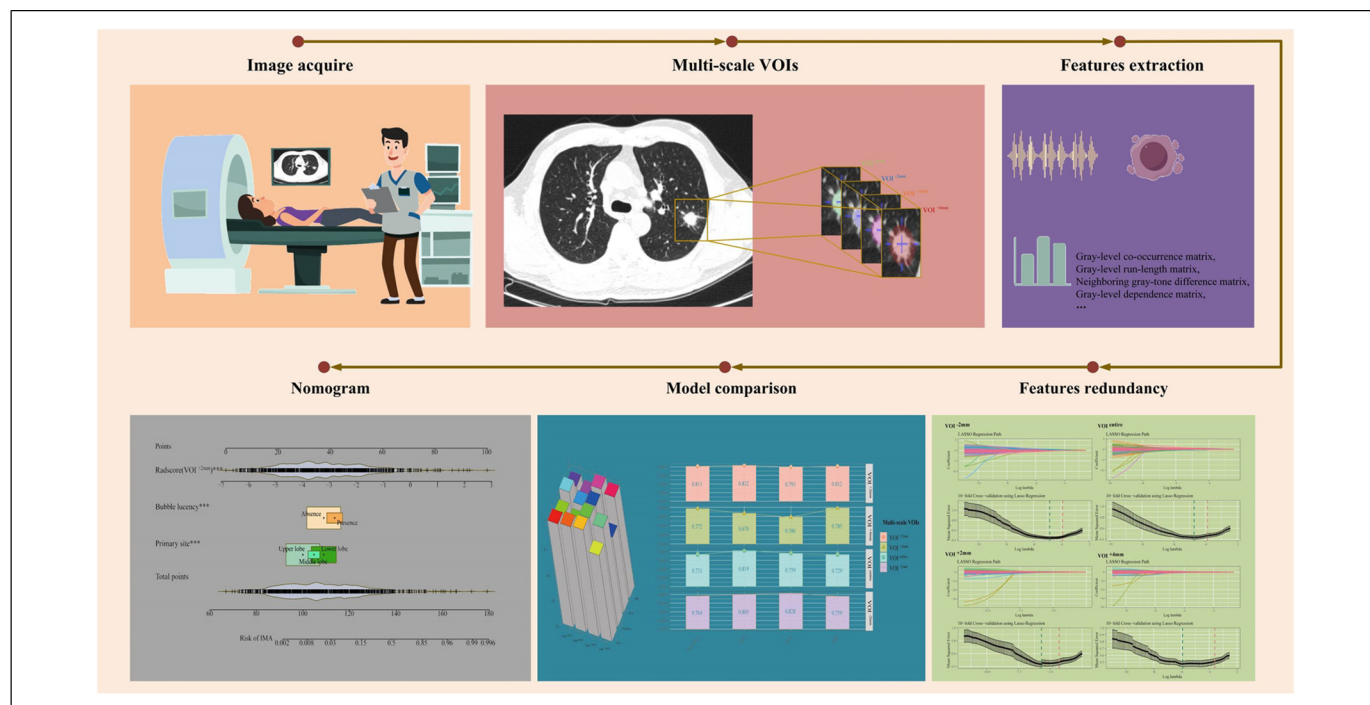


Figure 1. Flowchart depicting the workflow methodology employed in this study.

solitary LADCs who underwent surgical resection were identified at three medical institutions. According to postoperative pathology, IMA was identified by the presence of tumor cells, comprising foveolar (or goblet cell) and columnar cell types. These cells commonly display mucin inside and outside their cytoplasm, with nuclei located at the base. Furthermore, the tumor often induces mucus accumulation in the surrounding alveoli.³

The inclusion criteria were as follows: (1) nodules with diameters of 5–30 mm; (2) IMA or non-IMA diagnosed after surgery according to postoperative pathology reports; and (3) availability of complete thin-slice CT image within 14 days of the pathological diagnosis. The exclusion criteria were as follows: (1) administration of antitumor therapy before examination or pathological diagnosis and (2) postoperative pathology reports confirming multiple LADC lesions. The patient selection flowchart is presented in Supplementary Figure 1. The enrolled cohort was subsequently divided such that two-thirds of the cases were allocated to the training dataset and the remaining one-third to the validation dataset.

CT Examinations

Preoperative chest CT was performed at various medical centers using multidetector CT machines. XTCH utilized Revolution 256 CT (GE Healthcare, Chicago, IL, USA) or MX16 CT (Philips Healthcare Best, Netherlands). AH-SWMU employed uCT550 or CT760 (Shanghai United Healthcare, Shanghai, China). AH-GMU utilized speed VCT (GE Healthcare). The imaging procedure involved helical scanning in the supine position, with patients instructed to hold their breath, capturing

images from the upper lung to below the costophrenic angle. The CT images were reconstructed using a standard algorithm, with slice thicknesses and intervals varying from 0.55 to 0.625 mm. For details regarding CT image acquisition, please refer to Supplemental Digital Content 1.

Image-Finding Classifier

Figure 1 shows the study flowchart. Eligible CT images collected from the three centers were co-registered and stored in DICOM format. These files were subsequently imported into RadiAnt DICOM Viewer (<https://www.radiantviewer.com>) to visualize all enrolled lesions. This visualization was accomplished through multiplanar reconstruction and maximum-density projection. Two highly skilled cardiothoracic radiologists (XX and YY) comprehensively assessed all lesions. The assessment involved description of lesions using high-resolution CT images, considering the CT density (SN, SSN, and GGN) and shape as well as spiculation, boundary, lobulation, vascular convergence, vacuole, and pleural indentation signs. Consultation was undertaken to ensure consensus and consistency in evaluating the qualitative indicators.

Lesion Segmentation

Gross tumor volume was delineated using ITK-SNAP software (Version 4.0, www.itksnap.org). VOIs were drawn on the CT images using a lung-specific CT window with a window width of 1,500 HU and a window level of −500 HU. A cardiothoracic radiologist with 6 years of experience (XX) delineated the tumor margins and manually segmented the VOIs across

all two-dimensional sections of the lesion on a slice-by-slice basis, adhering to the tumor boundaries. This procedure established the complete VOI. Subsequently, the delineation was reviewed and refined by another radiologist (YY) with 22 years of expertise in the field. During segmentation, efforts were made to minimize the inclusion of vessels, bronchi, and pleura. Previous studies have shown that a 2–4-mm extension beyond the visible border indicates microscopic disease extension and represents an aggressive region, with no noticeable improvement in diagnostic performance.^{24,25}

In this study, a Python platform (Version 3.11) was utilized for pixel filtering through pixel thresholding to automatically exclude non-pulmonary tissues, such as peritumoral vessels, soft tissues, the chest wall, mediastinum, and abdominal structures, resulting in regions collectively defined as VOI^{entire}. Radial indentation or expansion was conducted at distances of −2, 2, and 4 mm from the tumor boundary; these subgroups were defined as VOI^{−2 mm}, VOI^{+2 mm}, and VOI^{+4 mm}, respectively.

Radiomic Feature Extraction

To ensure consistency and uniformity across the dataset, the original CT images were resampled to standardize the voxel spacing to $1 \times 1 \times 1 \text{ mm}^3$ (x, y, and z). This standardization was necessary because images were incorporated from multiple centers, and various CT protocols were utilized. Subsequently, 1239 radiomic features were extracted for each VOI. These features encompassed different measurements, including first-order statistics, shape-based metrics, gray-level run-length matrices, gray-dependence matrices, gray-level size matrices, gray-level co-occurrence matrices, and neighboring gray-tone difference matrices.

Radiomic Feature Redundancy

To normalize all radiomic feature intensities, we employed z-score transformation ($z = (x - \mu)/\sigma$). Following this, we applied the maximal redundancy minimal relevance (mRMR) algorithm, which aims to reduce feature dimensionality by selecting a subset of features that exhibit low redundancy and high correlation with the target variable. This process ultimately resulted in a more efficient and effective representation of the top 100 radiomic features. Next, we utilized the least absolute shrinkage and selection operator (LASSO) with a 10-fold cross-validation process to determine the optimal hyperparameter λ (Supplementary Figure 2) across the VOI^{entire}, VOI^{−2 mm}, VOI^{+2 mm}, and VOI^{+4 mm}. Features with nonzero coefficients under the optimal λ were then selected as the final candidate radiomic signature.

Data Balancing and Development of Radiomic Models

Following the dimensionality reduction of high-dimensional radiomics features, we advanced to the subsequent phase of data balancing. Due to the imbalanced distribution of IMA cases (8%, $n = 110$) compared to non-IMA cases (92%, $n = 1273$), there exists a potential for the models to exhibit bias

toward the majority group during the training process. To address this issue, we implemented resampling techniques, specifically employing the synthetic minority oversampling technique (SMOTE) using the “DMwR” package in R. This approach was utilized to rebalance the distribution within the training dataset for model development. Importantly, these resampling methods were applied exclusively to the training cohort, ensuring data integrity and preserving the representation of real clinical scenarios. We oversampled the minority class (IMA cases) at a ratio of 1:5 with the majority class to balance the minimal under-sampling of the majority class while achieving a better overall balance in the dataset. After applying SMOTE, the distribution balance of the label space (IMA or non-IMA) was significantly improved by oversampling the minority group (Supplementary Figure 3).

After the feature selection process, the Radscore was calculated by linearly combining the selected features with their corresponding weights using the following formula: Radscore = intercept + coefficient \times selected radiomic features. Based on the Radscore of the corresponding VOIs, radiomic models were developed for VOI^{entire}, VOI^{−2 mm}, VOI^{+2 mm}, and VOI^{+4 mm}.

Statistical Analysis

To assess the normality of the numeric variables, we conducted the Kolmogorov–Smirnov test. Normally distributed numeric variables were reported as means \pm standard deviations, and an independent samples *t*-test was performed to compare the two groups. For skewed data, the median, along with the 25th and 75th quartiles, was used, and the Mann–Whitney U test was employed for analysis. Categorical variables were analyzed using the chi-square test, with $P < .05$ considered statistically significant. To identify independent factors that distinguish IMA from non-IMA in IPNs, we conducted multivariate stepwise logistic regression analysis. Results were reported as odds ratios (ORs), 95% confidence intervals (CIs), and corresponding *P*-values. Importantly, measures were taken to avoid using consecutive identical phrases from the original text.

The models were trained using the training dataset, and the prediction results were validated with the validation dataset to prevent overfitting. Following this, we constructed a nomogram based on the regression coefficients obtained from the model. To assess the predictive capability of the model, we utilized receiver operating characteristic (ROC) curves to calculate the area under the curve (AUC) along with sensitivity (SEN) and specificity (SPE) values. A larger AUC value indicated better diagnostic performance of the model. Additionally, we conducted decision curve analysis (DCA) to identify potential clinical decision thresholds.

Results

Comparison of Baseline Characteristics

The present study enrolled 1383 patients with IPNs from three medical centers, among whom 110 (8%) were diagnosed with

Table 1. Comparative Analysis of Clinical-Radiological Features Between Training and Validation Datasets.

Variables	Total (n = 1383)	Training dataset (n = 922)	Validation dataset (n = 461)	P-value
Label, n (%)				.131
Non-IMA	1273 (92)	841 (91.2)	432 (93.7)	
IMA	110 (8)	81 (8.8)	29 (6.3)	
Sex, n (%)				.310
Female	894 (64.6)	587 (63.7)	307 (66.6)	
Male	489 (35.4)	335 (36.3)	154 (33.4)	
Age, Median (Q1, Q3)	57 (51, 66)	57 (51, 66)	58 (51, 66)	.349
Laterality, n (%)				.385
Left	570 (41.2)	388 (42.1)	182 (39.5)	
Right	813 (58.8)	534 (57.9)	279 (60.5)	
Primary site, n (%)				.236
Lower lobe	472 (34.1)	303 (32.9)	169 (36.7)	
Middle lobe	105 (7.6)	67 (7.3)	38 (8.2)	
Upper lobe	806 (58.3)	552 (59.9)	254 (55.1)	
Clinical T stage, n (%)				.945
cT1a	94 (6.8)	64 (6.9)	30 (6.5)	
cT1b	723 (52.3)	480 (52.1)	243 (52.7)	
cT1c	566 (40.9)	378 (41)	188 (40.8)	
CT density, n (%)				.487
GGN	580 (41.9)	390 (42.3)	190 (41.2)	
SN	449 (32.5)	305 (33.1)	144 (31.2)	
SSN	354 (25.6)	227 (24.6)	127 (27.5)	
Margin, n (%)				.801
Ill-defined	305 (22.1)	201 (21.8)	104 (22.6)	
Well-defined	1078 (77.9)	721 (78.2)	357 (77.4)	
Shape, n (%)				.245
Irregular	637 (46.1)	414 (44.9)	223 (48.4)	
Round/oval	746 (53.9)	508 (55.1)	238 (51.6)	
Lobulation, n (%)				.629
Absence	566 (40.9)	382 (41.4)	184 (39.9)	
Presence	817 (59.1)	540 (58.6)	277 (60.1)	
Spiculation, n (%)				.371
Absence	685 (49.5)	465 (50.4)	220 (47.7)	
Presence	698 (50.5)	457 (49.6)	241 (52.3)	
Vascular change, n (%)				.486
Absence	322 (23.3)	209 (22.7)	113 (24.5)	
Presence	1061 (76.7)	713 (77.3)	348 (75.5)	
Bubble lucency, n (%)				.050
Absence	1114 (80.5)	757 (82.1)	357 (77.4)	
Presence	269 (19.5)	165 (17.9)	104 (22.6)	
Pleural indentation, n (%)				.067
Absence	574 (41.5)	399 (43.3)	175 (38)	
Presence	809 (58.5)	523 (56.7)	286 (62)	

Abbreviation: GGN, ground-glass nodule; SN, solid nodule; SSN, subsolid nodule; IMA, invasive mucinous adenocarcinoma.

IMA. Of the 1383 patients, 922 were allocated to the training dataset, whereas the remaining 461 were assigned to the validation dataset. No significant disparities were identified between the training and validation datasets (Table 1).

Table 2 provides comprehensive information on IMA and non-IMA in patients with IPNs. Within the training dataset, compared with non-IMA, IMA showed a higher incidence of T stage ($P < .001$), CT density ($P < .001$), lobulation ($P = .018$), bubble lucency ($P < .001$), lower lobe predominance ($P < .001$), and irregular shape predominance ($P = .005$) in IPNs.

Performance of the multi-Scale VOI-Based Radiomic Model

LASSO regression-identified radiomic features were used to construct the Radscores for each VOI subgroup. Consequently, the $VOI^{-2 \text{ mm}^-}$, VOI^{entire^-} , $VOI^{+2 \text{ mm}^-}$, and $VOI^{+4 \text{ mm}^-}$ -based radiomic models were built with a final selection of 25, 30, 29, and 42 radiomic features, respectively, to construct the Radscore (Supplementary Figure 4). The results showed that IMA achieved higher Radscores in each VOI subgroup than non-IMA in IPNs (all $P < .001$) (Figure 2). The

Table 2. Comparative Analysis of Clinical-Radiological Features Between non-IMA and IMA Within the Training Dataset.

Variables	Total (n = 922)	Non-IMA (n = 841)	IMA (n = 81)	P-value
Sex, n (%)				.458
Female	587 (63.7)	539 (64.1)	48 (59.3)	
Male	335 (36.3)	302 (35.9)	33 (40.7)	
Age, Median (Q1, Q3)	57 (51, 66)	57 (51, 66)	60 (53, 67)	.121
Laterality, n (%)				.57
Left	388 (42.1)	351 (41.7)	37 (45.7)	
Right	534 (57.9)	490 (58.3)	44 (54.3)	
Primary site, n (%)				< .001
Lower lobe	303 (32.9)	253 (30.1)	50 (61.7)	
Middle lobe	67 (7.3)	60 (7.1)	7 (8.6)	
Upper lobe	552 (59.9)	528 (62.8)	24 (29.6)	
Clinical T stage, n (%)				< .001
cT1a	64 (6.9)	64 (7.6)	0 (0)	
cT1b	480 (52.1)	448 (53.3)	32 (39.5)	
cT1c	378 (41)	329 (39.1)	49 (60.5)	
CT density, n (%)				< .001
GGN	390 (42.3)	386 (45.9)	4 (4.9)	
SN	305 (33.1)	250 (29.7)	55 (67.9)	
SSN	227 (24.6)	205 (24.4)	22 (27.2)	
Margin, n (%)				.744
Ill-defined	201 (21.8)	185 (22)	16 (19.8)	
Well-defined	721 (78.2)	656 (78)	65 (80.2)	
Shape, n (%)				.005
Irregular	414 (44.9)	365 (43.4)	49 (60.5)	
Round/oval	508 (55.1)	476 (56.6)	32 (39.5)	
Lobulation, n (%)				.018
Absence	382 (41.4)	359 (42.7)	23 (28.4)	
Presence	540 (58.6)	482 (57.3)	58 (71.6)	
Spiculation, n (%)				.087
Absence	465 (50.4)	432 (51.4)	33 (40.7)	
Presence	457 (49.6)	409 (48.6)	48 (59.3)	
Vascular change, n (%)				.383
Absence	209 (22.7)	187 (22.2)	22 (27.2)	
Presence	713 (77.3)	654 (77.8)	59 (72.8)	
Bubble lucency, n (%)				< .001
Absence	757 (82.1)	707 (84.1)	50 (61.7)	
Presence	165 (17.9)	134 (15.9)	31 (38.3)	
Pleural indentation, n (%)				.404
Absence	399 (43.3)	368 (43.8)	31 (38.3)	
Presence	523 (56.7)	473 (56.2)	50 (61.7)	

Abbreviation: GGN, ground-glass nodule; SN, solid nodule; SSN, subsolid nodule; IMA, invasive mucinous adenocarcinoma.

VOI^{+2 mm}-based radiomic model had the highest performance, with an AUC of 0.832 (0.753-0.911), followed by the VOI^{entire}-based radiomic model with an AUC of 0.819 (0.751-0.887), the VOI^{-2 mm}-based radiomic model with an AUC of 0.805 (0.708-0.903), and the VOI^{+4 mm}-based radiomic model with an AUC of 0.670 (0.546-0.793) (Table 3). The performance metrics of AUC, accuracy, SEN, and SPE of all models are presented in Figure 3.

Application of the Combined Nomogram

After applying the selected image-finding classifier and optimal VOI subgroup (VOI^{-2 mm}-based) radiomic models to discriminate between IMA and non-IMA preoperatively in patients with IPNs, we identified the following independent predictive

factors: primary site (ref. lower lobe) (OR, 0.931 [0.899-0.964], $P < .001$), bubble lucency (ref. absence) (OR, 1.062 [1.018-1.108], $P = .006$), and Radscore (VOI^{+2 mm}) (OR, 1.1 [1.084-1.115], $P < .001$) (Table 4). Following multivariate logistic regression analysis, we constructed a combined nomogram that visually simplified the complex regression equation to predict the probability of IMA (Figure 4).

Calibration analysis (Hosmer–Lemeshow test, $P = .42$) confirmed a strong correspondence between the predicted and actual values for the risk of IMA (Figure 5). This finding further indicates that the combined nomogram had good calibration ability. Furthermore, the ROC (Figure 6a) and DCA (Figure 6b) curves demonstrated the strong discriminative ability and clinical benefits of the combined nomogram. The ROC curve (Figure 6a) showed that the combined nomogram

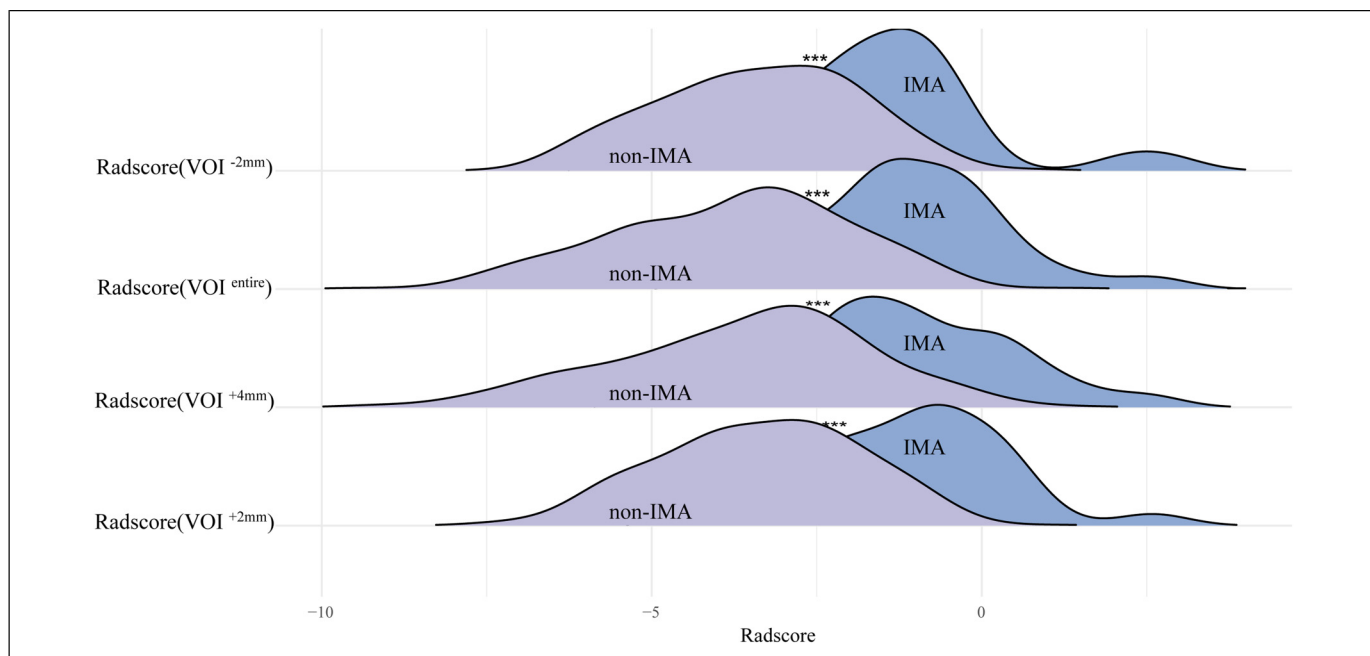


Figure 2. Ridge plots presenting the comparison of Radscores across VOI^{-2mm}-, VOI^{entire}-, VOI^{+2mm}-, and VOI^{+4mm}-based radiomic models. VOI, volume of interest.

Table 3. Performance Evaluation of Radiomics Models Utilizing Multi-scale VOIs for Predicting IMA.

Models	AUC	Accuracy	SEN	SPE
VOI ^{-2mm} -based radiomics model	0.805 (0.708-0.903)	0.764 (0.763-0.764)	0.828 (0.690-0.965)	0.759 (0.719-0.800)
VOI ^{-entire} -based radiomics model	0.819 (0.751-0.887)	0.731 (0.730-0.732)	0.759 (0.603-0.914)	0.729 (0.687-0.771)
VOI ^{+2mm} -based radiomics model	0.832 (0.753-0.911)	0.811 (0.811-0.812)	0.793 (0.646-0.941)	0.812 (0.776-0.849)
VOI ^{+4mm} -based radiomics model	0.670 (0.546-0.793)	0.772 (0.771-0.773)	0.586 (0.407-0.765)	0.785 (0.746-0.823)

Abbreviation: AUC, Area under curve; SEN, Sensitivity; SPE, Specificity; VOI, Volume of internet; IMA, Invasive mucinous adenocarcinoma; SPN, solitary pulmonary nodules.

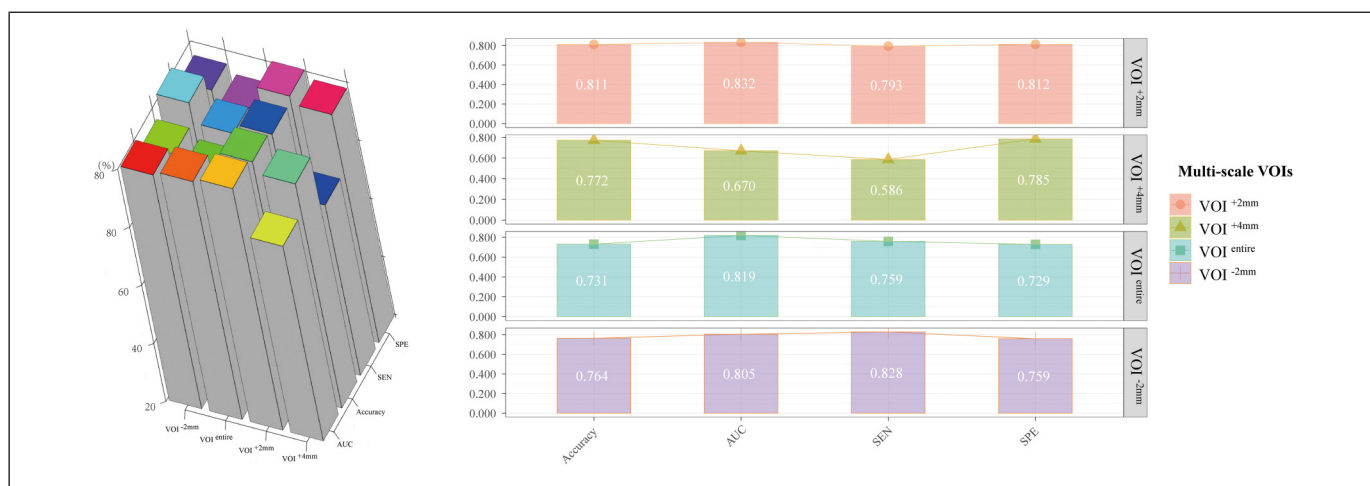


Figure 3. Visualization of performance metrics, including AUC, SEN, and SPE. AUC, area under the curve; SEN, sensitivity; SPE, specificity.

had the highest AUC of 0.850 (0.776-0.925), followed by the $\text{VOI}^{+2\text{ mm}}$ -based radiomic model with an AUC of 0.832 (0.753-0.911) and imaging findings with an AUC of 0.684 (0.568-0.801). Additional details regarding AUC, accuracy, SEN, and SPE values for the combined nomogram, radiomics, and imaging findings are provided in Table 5. Moreover, DCA (Figure 6b) indicated that the combined nomogram exhibited a superior risk threshold probability, compared with the $\text{VOI}^{+2\text{ mm}}$ -based radiomic or image-finding classifier, across a wide interval.

Discussion

Our multicenter, large-scale study included a multi-scale VOI subgroup-based radiomic analysis to differentiate between

IMA and non-IMA in patients with IPNs preoperatively. Our findings indicate that extracting radiomic features from the intertumoral region and extending to 2 mm of surrounding parenchyma enhances the differentiation between IMA and non-IMA in IPNs, outperforming the other VOI subgroups. The image-finding classifier, which includes bubble lucency and lower lobe predominance, remained an independent predictor for differentiating between IMA and non-IMA in IPNs. Combining the $\text{VOI}^{+2\text{ mm}}$ -based radiomic model with the image-finding classifier produced a combined nomogram demonstrating remarkable predictive performance with strong discriminative and calibration abilities.

The study findings indicate that bubble lucency and lower lobe predominance are crucial for establishing an image-finding classifier to differentiate between IMA and non-IMA in patients with IPNs. IMA has been associated with susceptibility to cavity lesions, where mucus is expelled from mucus pools through the attached bronchi. This leads to invasive tumor growth along the terminal airway, with mucus secretion inhibiting respiratory valve-like function, resulting in air cavity formation due to alveolar rupture after overinflation. Moreover, tumor-free areas comprising normal alveolar cavities are formed, whereas hydrolase degradation within tumors destroys these air cavities formed by normal alveolar interstitial elastic fibers.¹⁴ Furthermore, Miyata et al²⁶ delineated diagnostic imaging hallmarks indicating early mucinous adenocarcinomas presenting as SN or SSN with air-containing spaces on CT. Previous studies also consider bubble lucency to be a crucial CT image finding for identifying IMA, consistent with our findings.^{19,27}

Moreover, our study highlights lower lobe predominance as another essential imaging characteristic for differentiating

Table 4. Multivariate Logistic Regression for Preoperatively Predicting IMA in IPNs.

Variables	Odd Ratio (95%CI)	P-value
Shape (ref. Irregular)	0.977(0.941-1.014)	.216
Lobulation (ref. Absence)	0.992(0.955-1.032)	.701
Bubble lucency (ref. Absence)	1.062(1.018-1.108)	.006
Primary site (ref. Lower lobe)	0.952(0.892-1.016)	.136
Primary site (ref. Lower lobe)	0.931(0.899-0.964)	<.001
CT density (ref. GGN)	0.952(0.906-1.001)	.053
CT density (ref. GGN)	0.963(0.92-1.008)	.103
Clinical T stage (ref. cT1a)	0.969(0.908-1.035)	.348
Clinical T stage (ref. cT1a)	0.937(0.874-1.006)	.072
Radscore ($\text{VOI}^{+2\text{ mm}}$)	1.1(1.084-1.115)	<.001

Abbreviation: IMA, Invasive mucinous adenocarcinoma; IPN, incidental pulmonary nodules; VOI, volumes of interest.

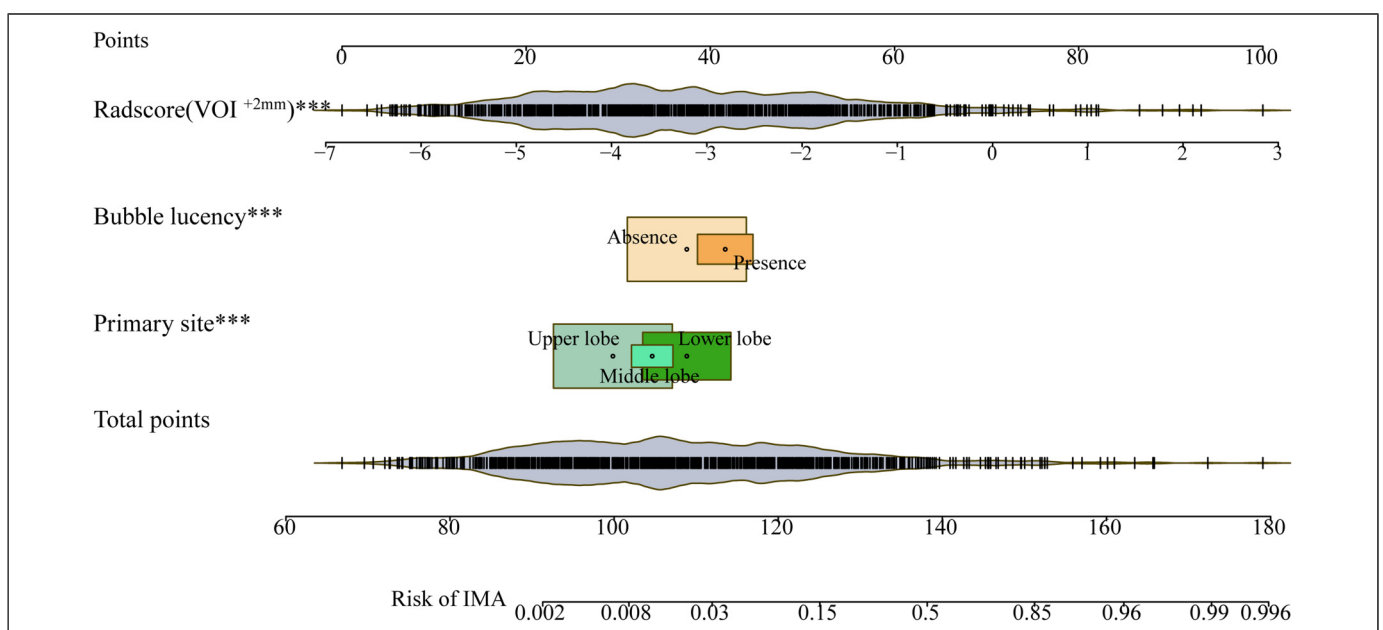


Figure 4. Combined nomogram visually simplifying the complex regression equation for predicting IMA probability. IMA, invasive mucinous adenocarcinoma.

between IMA and non-IMA. This distinction may be linked to the pathogenesis, as IMA tumor cells are derived from goblet or columnar epithelial cells.³ With their mucin-secreting function, these cells produce increased mucus during cancer progression. Because of gravity, these cancerous cells and excess mucus tend to move downward, leading to a higher propensity for mucinous adenocarcinomas to develop in the lower lobe, consistent with previous findings.^{16,19}

Although the image-finding classifier, which includes bubble lucency and lower lobe predominance, remained an independent predictor for differentiating between IMA and non-IMA in IPNs, it exhibited low diagnostic efficacy with an AUC of 0.684 (0.568-0.801). This may be because these imaging findings, assessed visually by radiologists, could not

fully capture tumor heterogeneity or the tumor microenvironment. Therefore, to explore the impact of multi-scale intertumoral and peritumoral ranges on preoperative IMA prediction,^{18,21-23} $VOI^{-2\text{ mm-}}$, $VOI^{\text{entire-}}$, $VOI^{+2\text{ mm-}}$, and $VOI^{+4\text{ mm-}}$ -based radiomic models were constructed.

Considering the imbalanced distribution of IMA (8%, 110) and non-IMA (92%, 1273) cases, IMA was classified as the minority class. This imbalance may lead to models exhibiting a bias towards the majority group during training. To counteract this issue, the SMOTE oversampling technique was employed. This technique generates extra samples for the minority class, thereby augmenting their presence in the dataset. Thus, our model can delve deeper into the characteristics of the minority class, ultimately bolstering its robustness. Consequently, the false-negative rate is significantly reduced, and the model's predictive performance is enhanced.²⁰ In this study, the $VOI^{+2\text{ mm-}}$ -based radiomic model exhibited the highest performance among the multi-scale VOI-based radiomic models, with an AUC of 0.832 (0.753-0.911), surpassing the image-finding classifier. This study emphasized that extending the analysis to the peritumoral region of 2 mm provided no additional benefit for differentiating between IMA and non-IMA. The performance variability of VOI subgroups in radiomic features could be due to the inclusion of peritumoral parenchyma, which reflects pathobiological factors such as invasion patterns, inflammation, and potential micrometastasis. Similarly, Wu et al²⁴ concluded that extending the analysis to the 5-mm peritumoral region did not enhance performance, compared with the 2-mm region, in differentiating invasive adenocarcinoma from adenocarcinoma *in situ* or minimally invasive adenocarcinoma. Furthermore, another study²⁸ revealed that the radiomic characteristics of the surrounding parenchyma did not improve the performance of the diagnostic model in distinguishing between benign and malignant solid pulmonary nodules measuring <2 cm in diameter.

To comprehensively assess tumor heterogeneity and enhance the accuracy of differentiation between IMA and non-IMA in

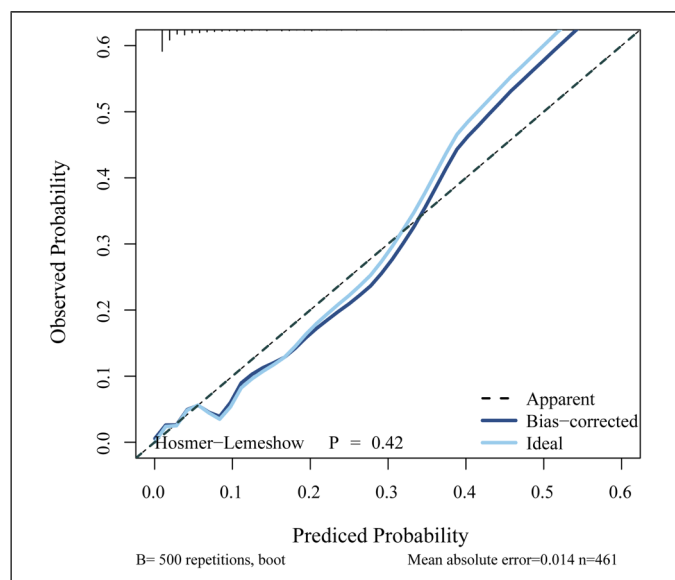


Figure 5. Calibration curve illustrating the performance of the combined nomogram.

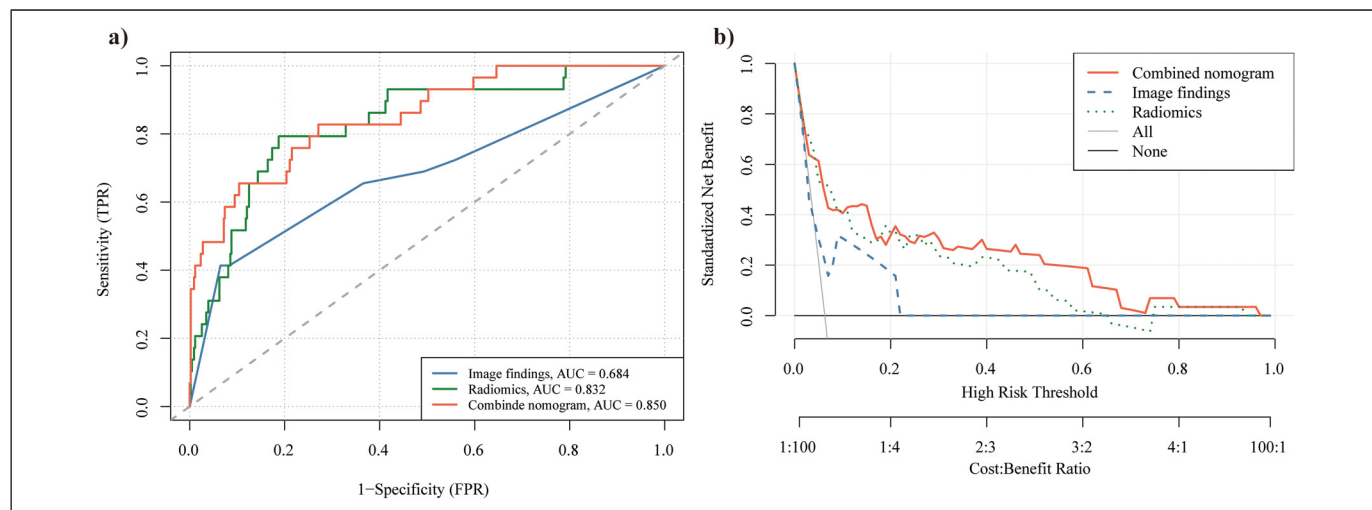


Figure 6. ROC(a) and DCA(b) curves of the combined nomogram. DCA, decision curve analysis; ROC, receiver operating characteristic.

Table 5. Performance Evaluation of Radiomics Models Utilizing VOI +2-based Radiomics, Image Finding, and Combined Nomogram for Predicting IMA.

Models	AUC (95%CI)	Accuracy(95%CI)	SEN (95%CI)	SPE (95%CI)
Image finding	0.684 (0.568-0.801)	0.902 (0.902-0.903)	0.414 (0.235-0.593)	0.935 (0.912-0.958)
VOI +2 ^{mm} -based radiomics	0.832 (0.753-0.911)	0.811 (0.811-0.812)	0.793 (0.646-0.941)	0.812 (0.776-0.849)
Combined nomogram	0.850 (0.776-0.925)	0.735 (0.735-0.736)	0.828 (0.690-0.965)	0.729 (0.687-0.771)

Abbreviation: AUC, Area under curve; SEN, Sensitivity; SPE, Specificity; VOI, Volume of interest; IMA, Invasive mucinous adenocarcinoma; SPN, solitary pulmonary nodules.

IPNs, we developed a combined nomogram integrating a multi-scale radiomic model and recognized imaging findings classifier. This combined nomogram exhibited superior performance, compared with using VOI +2^{mm}-based radiomic or imaging findings independently, providing a more comprehensive and multidimensional range of information. Integrating multi-scale radiomics information into prediction models underscores the clinical significance of our approach and offers enhanced diagnostic capabilities.

In conclusion, this multicenter, large-scale study explored a multi-scale radiomics model for differentiating between IMA and non-IMA in IPNs. The SMOTE technique was employed to address the data imbalance issue, thereby enhancing the model's robustness. Our findings indicate that, among the various multi-scale radiomic models tested, the VOI +2^{mm}-based radiomic model achieved the highest diagnostic efficiency. Furthermore, the combined nomogram, which integrates the VOI +2^{mm}-based radiomic model with recognized imaging findings, demonstrated the highest accuracy in predicting IMA. Overall, preoperative prediction of IMA may assist physicians in devising comprehensive treatment strategies.

Limitations of the Study

This study has shown promising results but has some limitations. First, the retrospective nature of our research may have introduced potential selection bias, as we only included patients with postoperative pathological results. Second, the relatively low incidence of IMA in our study may be due to its rarity despite the SMOTE algorithm being used to rebalance the distribution for model development. Third, the limited postoperative follow-up duration prevented the development of a prognostic model for disease outcomes. Fourth, our investigation was specifically focused on distinguishing between IMA and non-IMA in IPNs, which may limit the generalizability of our results to other disease stages. Therefore, in the future, we plan to conduct a broader range of studies on other disease stages and imaging phenotypes to ensure the credibility and applicability of our analyses beyond the scope of the current investigation.

Acknowledgments

We would like to extend our sincere appreciation to Editage for their meticulous language editing services, which have significantly enhanced the quality and readability of this manuscript.

Author Contributions

Z.Z. and G.Z. wrote the manuscript. X.F. and S.Z. designed the research. J.C., Q.X., Y.Z., W.G., W.Q., L.Y., and H.L. performed the research. J.C., Q.X., and S.L. analyzed the data. J.C., Y.Z., W.G., W.Q., L.Y., and H.L. directly accessed and verified the underlying data reported in the manuscript. X.F. and S.Z. were responsible for the decision to submit the manuscript. All authors read and approved the final version of the manuscript.

Data Availability

The data that support the findings of this study are available on request from the corresponding author. The data are not publicly available due to privacy or ethical restrictions.

Declaration of Conflicting Interests

The authors declared no potential conflicts of interest with respect to the research, authorship, and/or publication of this article.

Funding


This work was supported by The National Key R&D Program of China (2022YFC2407404); Special Research Fund for Central Universities, Peking Union Medical College (2022-I2M-C&T-B-065, 2022-I2M-C&T-B-060); National High-Level Hospital Clinical Research Funding (2022-PUMCH-A-018, 2022-PUMCH-C-043); Beijing Municipal Science & Technology Commission (Z211100002921058); Beijing Natural Science Foundation (7232134; J20010); Beijing Hope Run Special Fund of Cancer Foundation of China (LC2021L01); and Sichuan Science and Technology Program (2022YFS0616).

Ethical Approval and Informed Consent Statements

The authors are accountable for all aspects of the work in ensuring that questions related to the accuracy or integrity of any part of the work are appropriately investigated and resolved. This study was conducted at three centres: National Cancer Center/National Clinical Research Center for Cancer/Cancer Hospital, The Affiliated

Hospital of Southwest Medical University and Xiangtan Central Hospital. The study was approved by the Ethics Committees of the participating hospitals (reference numbers: KY2020147, 2021-07-009, and 22/244-3446) following the Declaration of Helsinki. All research procedures strictly adhered to the relevant guidelines and regulations, and written informed consent was obtained from all participants.

ORCID iD

Zhichao Zuo  <https://orcid.org/0009-0004-4824-6138>

Supplemental Material

Supplemental material for this article is available online.

References

- Leiter A, Veluswamy RR, Wisnivesky JP. The global burden of lung cancer: Current status and future trends. *Nat Rev Clin Oncol.* 2023;20(9):624-639.
- Travis WD, Brambilla E, Noguchi M, et al. American Thoracic society. International association for the study of lung cancer/ American thoracic society/European respiratory society: International multidisciplinary classification of lung adenocarcinoma: Executive summary. *J Thorac Oncol.* 2011;6(2):244-285.
- Chang WC, Zhang YZ, Nicholson AG. Pulmonary invasive mucinous adenocarcinoma. *Histopathology.* 2024;84(1):18-31.
- Travis WD, Brambilla E, Nicholson AG, et al. The 2015 world health organization classification of lung tumors: Impact of genetic, clinical and radiologic advances since the 2004 classification. *J Thorac Oncol.* 2015;10(9):1243-1260.
- Duruiseaux M, Antoine M, Rabbe N, et al. The impact of intracytoplasmic mucin in lung adenocarcinoma with pneumonic radiological presentation. *Lung Cancer.* 2014;83(3):334-340.
- Yoon HJ, Kang J, Lee HY, et al. Recurrence dynamics after curative surgery in patients with invasive mucinous adenocarcinoma of the lung. *Insights Imaging.* 2022;13(1):64.
- Warth A, Muley T, Kossakowski CA, et al. Prognostic impact of intra-alveolar tumor spread in pulmonary adenocarcinoma. *Am J Surg Pathol.* 2015;39(6):793-801.
- Shim HS, Kenudson M, Zheng Z, et al. Unique genetic and survival characteristics of invasive mucinous adenocarcinoma of the lung. *J Thorac Oncol.* 2015;10(8):1156-1162.
- Kadota K, Yeh YC, Angelo D, et al. Associations between mutations and histologic patterns of mucin in lung adenocarcinoma: Invasive mucinous pattern and extracellular mucin are associated with KRAS mutation. *Am J Surg Pathol.* 2014;38(8):1118-1127.
- Guo M, Tomoshige K, Meister M, et al. Gene signature driving invasive mucinous adenocarcinoma of the lung. *EMBO Mol Med.* 2017;9(4):462-481.
- Shang G, Jin Y, Zheng Q, et al. Histology and oncogenic driver alterations of lung adenocarcinoma in Chinese. *Am J Cancer Res.* 2019;9(6):1212-1223.
- Lee HY, Cha MJ, Lee KS, et al. Prognosis in resected invasive mucinous adenocarcinomas of the lung: Related factors and comparison with resected nonmucinous adenocarcinomas. *J Thorac Oncol.* 2016;11(7):1064-1073.
- Matsui T, Sakakura N, Koyama S, et al. Comparison of surgical outcomes between invasive mucinous and non-mucinous lung adenocarcinoma. *Ann Thorac Surg.* 2021;112(4):1118-1126.
- Beck KS, Sung YE, Lee KY, Han DH. Invasive mucinous adenocarcinoma of the lung: Serial CT findings, clinical features, and treatment and survival outcomes. *Thorac Cancer.* 2020;11(12):3463-3472.
- Nie K, Nie W, Zhang YX, Yu H. Comparing clinicopathological features and prognosis of primary pulmonary invasive mucinous adenocarcinoma based on computed tomography findings. *Cancer Imaging.* 2019;19(1):47.
- Wang T, Yang Y, Liu X, et al. Primary invasive mucinous adenocarcinoma of the lung: Prognostic value of CT imaging features combined with clinical factors. *Korean J Radiol.* 2021;22(4):652-662.
- Bonney A, Malouf R, Marchal C, et al. Impact of low-dose computed tomography (LDCT) screening on lung cancer-related mortality. *Cochrane Database Syst Rev.* 2022;8(8):Cd013829.
- Chen M, Copley SJ, Viola P, Lu H, Aboagye EO. Radiomics and artificial intelligence for precision medicine in lung cancer treatment. *Semin Cancer Biol.* 2023;93:97-113.
- Zhang J, Hao L, Li M, Xu Q, Shi G. CT Radiomics combined with clinicopathological features to predict invasive mucinous adenocarcinoma in patients with lung adenocarcinoma. *Technol Cancer Res. Treat.* 2023;22:15330338231174306.
- Xiao Z, Chen J, Feng X, et al. Use of CT-derived radiomic features to preoperatively identify invasive mucinous adenocarcinoma in solitary pulmonary nodules ≤ 3 cm. *Heliyon.* 2024;10(9):e30209.
- Chen Q, Shao J, Xue T, et al. Intratumoral and peritumoral radiomics nomograms for the preoperative prediction of lymphovascular invasion and overall survival in non-small cell lung cancer. *Eur Radiol.* 2023;33(2):947-958.
- Wang X, Zhao X, Li Q, et al. Can peritumoral radiomics increase the efficiency of the prediction for lymph node metastasis in clinical stage T1 lung adenocarcinoma on CT? *Eur Radiol.* 2019;29(11):6049-6058.
- Shang Y, Chen W, Li G, et al. Computed tomography-derived intratumoral and peritumoral radiomics in predicting EGFR mutation in lung adenocarcinoma. *Radiol Med.* 2023;128(12):1483-1496.
- Wu L, Gao C, Ye J, et al. The value of various peritumoral radiomic features in differentiating the invasiveness of adenocarcinoma manifesting as ground-glass nodules. *Eur Radiol.* 2021;31(12):9030-9037.
- Liu K, Li K, Wu T, et al. Improving the accuracy of prognosis for clinical stage I solid lung adenocarcinoma by radiomics models covering tumor per se and peritumoral changes on CT. *Eur Radiol.* 2022;32(2):1065-1077.
- Miyata N, Endo M, Nakajima T, et al. High-resolution computed tomography findings of early mucinous adenocarcinomas and their pathologic characteristics in 22 surgically resected cases. *Eur J Radiol.* 2015;84(5):993-997.
- Zhang X, Qiao W, Kang Z, et al. CT Features of stage IA invasive mucinous adenocarcinoma of the lung and establishment of a prediction model. *Int J Gen Med.* 2022;15:5455-5463.
- Wu S, Zhang N, Wu Z, Ren J, Linning E. Can peritumoral radiomics improve the prediction of malignancy of solid pulmonary nodule smaller than 2cm? *Acad Radiol.* 2022;29(Suppl 2):S47-s52.